Automatica 159 (2024) 111367

Contents lists available at ScienceDirect

Automatica

journal homepage: www.elsevier.com/locate/automatica

Brief paper

Saturated adaptive pose tracking control of spacecraft on SE(3) under attitude constraints and obstacle-avoidance constraints ☆

Zeyu Kang [a], Qiang Shen [a,*], Shufan Wu [a], Christopher J. Damaren [b]

[a] The school of Aeronautics and Astronautics, Shanghai Jiao Tong University, Shanghai, 200240, China
[b] The Institute for Aerospace Studies, University of Toronto, Toronto, Ontario, M3H 5T6, Canada

ARTICLE INFO

Article history:
Received 23 August 2022
Received in revised form 27 July 2023
Accepted 26 September 2023
Available online xxxx

Keywords:
Attitude constraint
Obstacle-avoidance constraint
Potential function
Input saturation

ABSTRACT

In this paper, for a translation and rotation coupled spacecraft, a saturated adaptive pose controller is proposed to achieve the desired pose configuration tracking under the attitude constraints and obstacle-avoidance constraints, input saturation, and external disturbances. First, a set of relative kinematics and dynamics of a spacecraft on SE(3) under input saturation is established. Second, cancellable potential functions are designed for the attitude constraints and the obstacle-avoidance constraints by introducing the warning range. Then, based on the uniformly asymptotically stable theory of nonlinear vanishing perturbation systems, an integrated pose controller leveraging the cancellable potential functions is proposed for the spacecraft on SE(3) to achieve the desired pose configuration tracking under multiple constraints. Finally, the effectiveness of the proposed integrated pose controller is illustrated by a numerical simulation of a spacecraft on SE(3) tracking the desired pose configuration under multiple constraints.

1. Introduction

In recent years, space technology has developed rapidly with the increasing frequency of human space missions, such as on-orbit precision operation, rendezvous and docking (RVD), complex spacecraft formation flying, space target capture, deep space exploration and so on. There is a need for higher requirements on the reliability, accuracy and rapidity of the translation and rotation couple spacecraft control system to cope with the emergence of various complex their space missions.

The traditional methods of designing attitude controller and translational controller respectively are powerless in the face of high complexity and precision space missions, which affects the control effect. Therefore, it is of important research significance to devise the integrated modeling and control of spacecraft position and attitude. Previous studies have developed many modeling methods for rigid body pose (position and attitude) control, including the dual quaternions (Gui & Vukovich, 2016) and the Lie group SE(3) (Brás, Izadi, Silvestre, Sanyal, & Oliveira, 2016; Hamrah & Sanyal, 2022), as well as other rotation and position vector combination methods of Euler angles (Kristiansen, Nicklasson, & Gravdahl, 2008), quaternions (Sun & Huo, 2015) and modified Rodriguez parameters (Sun, Sun, & Jiang, 2022). The dual quaternions and the Lie group SE(3) are more compact than other methods. However, the fuzziness of the dual quaternions results in the same attitude being expressed by two different quaternions (Guo, Song, & Li, 2016). The pose model of spacecraft on SE(3) can avoid this problem, which has attracted extensive research recently (Dhullipalla, Hamrah, Warier, & Sanyal, 2019; Lee, Viswanathan, Holguin, Sanyal, & Butcher, 2013; Zhang, Ye, Xiao, & Sun, 2022).

In addition, the spacecraft may be faced with the threat of collision with other spacecraft, targets and space obstacles (Hu, Dong, Zhang, & Ma, 2015). Meanwhile, the spaceborne equipment on the spacecraft needs to meet attitude constraints (Li, Wang, Zhang, & Duan, 2021). Recently, plenty of research efforts are devoted to the RVD of spacecraft, which considers both attitude constraints and obstacle-avoidance constraints. In Zappulla, Park, Virgili-Llop, and Romano (2019), considering the dynamic environment, the autonomous RVD of spacecraft was realized based on the artificial potential functions. In Henry, Zenteno-Torres, Cieslak, Ferreira De Loza, and Dávila (2021), a spacecraft modeled as a translation and rotation coupled model was established on dual quaternions, and a fault-tolerant controller was designed to realize the autonomous RVD. However, the above research only focuses on the special scene of spacecraft RVD, and cannot be

☆ This work was supported in part by the National Natural Science Foundation of China under Grant, No. 62103275, No. U20B2054, No. U20B2056. The material in this paper was not presented at any conference. This paper was recommended for publication in revised form by Associate Editor Francesco Vasca under the direction of Editor Thomas Parisini.

* Corresponding author.
E-mail addresses: kangzeyu@sjtu.edu.cn (Z. Kang), qiangshen@sjtu.edu.cn (Q. Shen), shufan.wu@sjtu.edu.cn (S. Wu), damaren@utias.utoronto.ca (C.J. Damaren).

https://doi.org/10.1016/j.automatica.2023.111367
0005-1098/

applied to spacecraft pose control under attitude constraints and obstacle-avoidance constraints.

To the best of our knowledge, for the spacecraft with pose constraints, nonlinear input saturation, and external disturbances, designing an integrated pose tracking controller on SE(3) is still an open problem. We address these challenging issues by establishing relative kinematics and dynamics of the spacecraft on SE(3) firstly. To handle the actuators saturation, an input saturation model is constructed with a dead-zone based operation. Then, cancellable potential functions (the potential functions are cancelled or does not work when the spacecraft reaches the desired pose configuration) for the attitude constraints and the obstacle-avoidance constraints are designed by introducing the warning range. Finally, based on the uniformly asymptotically stable theory of nonlinear vanishing perturbation systems (Khalil, 2002, Section 9.1), an saturated adaptive pose (SAP) controller using the cancellable potential functions is proposed for the spacecraft to achieve the desired pose configuration tracking under multiple constraints.

The main contributions of this work are summarized as:

1. In contrast to the existing attitude potential functions in Chen and Shan (2021), Kulumani and Lee (2017) and Shen, Yue, Goh, Wu, and Wang (2018), the proposed attitude potential function, considers not only the static attitude-forbidden zones, but also the dynamic attitude-forbidden zones. In addition, we also proposed a method for calculating the warning angle and warning distance and applied these to the design of potential functions.
2. Compared with Huang, Yan, and Zhou (2017), Huang, Yan, Zhou, and Yang (2017) and Zhang, Ye, Biggs, and Sun (2019), the uniformly asymptotically stable theory of nonlinear vanishing perturbation systems is rigorously applied for the closed-loop stability analysis, where we obtain a conservative condition for satisfying the key requirement in the theory by using saturation operation.

2. Preliminaries

2.1. Kinematics and dynamics of a spacecraft on SE(3)

In this paper, a translation and rotation coupled spacecraft is considered. Let $\mathcal{I}(\boldsymbol{x}_I, \boldsymbol{y}_I, \boldsymbol{z}_I)$ denote the Earth centered inertial (ECI) frame and $\mathcal{B}(\boldsymbol{x}_b, \boldsymbol{y}_b, \boldsymbol{z}_b)$ denote the body-fixed frame with the origin being located at the centroid. Let $\boldsymbol{p} \in \mathbb{R}^3$ express the position vector of the spacecraft in the ECI frame $\mathcal{I}$ and $\boldsymbol{R} \in \mathrm{SO}(3)$ express the spacecraft rotation matrix from body-fixed frame $\mathcal{B}$ to ECI frame $\mathcal{I}$. The rotation matrix $\boldsymbol{R} \in \mathrm{SO}(3)$ is a special Euclidean group used to parameterize attitude and is defined as (Yue et al., 2023) $\mathrm{SO}(3) = \{\boldsymbol{R} \in \mathbb{R}^{3\times3} \mid \boldsymbol{R}^{\mathrm{T}}\boldsymbol{R} = \boldsymbol{I}_3, \det(\boldsymbol{R}) = 1\}$. Then, a Lie group SE(3) can be represented by the semidirect product $\mathrm{SE}(3) = \mathbb{R}^3 \ltimes \mathrm{SO}(3)$, and an element $\boldsymbol{g} \in \mathbb{R}^{4\times4}$ of the Lie group SE(3) and the corresponding inverse matrix $\boldsymbol{g}^{-1} \in \mathbb{R}^{4\times4}$ with the form

$$\boldsymbol{g} = \begin{bmatrix} \boldsymbol{R} & \boldsymbol{p} \\ \boldsymbol{0}_{1\times3} & 1 \end{bmatrix}, \quad \boldsymbol{g}^{-1} = \begin{bmatrix} \boldsymbol{R}^{\mathrm{T}} & -\boldsymbol{R}^{\mathrm{T}}\boldsymbol{p} \\ \boldsymbol{0}_{1\times3} & 1 \end{bmatrix}, \tag{1}$$

can be used to compactly represent the pose configuration of a spacecraft (Lee & Vukovich, 2016). The kinematics of a spacecraft can be given as (Brás et al., 2016)

$$\dot{\boldsymbol{g}} = \boldsymbol{g}\hat{\boldsymbol{\xi}}, \quad \text{with} \quad \hat{\boldsymbol{\xi}} = \begin{bmatrix} \boldsymbol{\omega}^{\times} & \boldsymbol{v} \\ \boldsymbol{0}_{1\times3} & 0 \end{bmatrix} \in \mathbb{R}^{4\times4}, \tag{2}$$

where $\hat{\boldsymbol{\xi}} \in \mathfrak{se}(3)$ is the isomorphism from vector space to Lie algebra associated with SE(3), $\boldsymbol{\xi} = [\boldsymbol{\omega}^{\mathrm{T}}, \boldsymbol{v}^{\mathrm{T}}]^{\mathrm{T}} \in \mathbb{R}^6$. $\boldsymbol{\omega} \in \mathbb{R}^3$ and $\boldsymbol{v} \in \mathbb{R}^3$ are the angular and the translational velocity vector of the spacecraft with respect to the ECI frame $\mathcal{I}$ and expressed in the body-fixed frame $\mathcal{B}$, respectively. $(\cdot)^{\times}$ is used to convert a vector in $\mathbb{R}^3$ to a 3×3 skew-symmetric matrix (cf. Kang, Shen, Wu, & Damaren, 2023, Eq. (3)).

Then, the translational and rotational equations of a spacecraft are given by (Mei, Liao, Gong, & Luo, 2022)

$$\boldsymbol{\Xi}\dot{\boldsymbol{\xi}} = \mathrm{ad}^*_{\boldsymbol{\xi}}\boldsymbol{\Xi}\boldsymbol{\xi} + \boldsymbol{\Gamma}_g(\boldsymbol{\Xi}) + \boldsymbol{\Gamma}_D + \boldsymbol{\Gamma}_c, \tag{3}$$

with

$$\begin{aligned} &\boldsymbol{\Xi} = \mathrm{diag}(\boldsymbol{J}, m\boldsymbol{I}_3) \in \mathbb{R}^{6\times6}, \ \boldsymbol{\Gamma}_g(\boldsymbol{\Xi}) = [\boldsymbol{M}_g^{\mathrm{T}}, \boldsymbol{F}_g^{\mathrm{T}}]^{\mathrm{T}} \in \mathbb{R}^6, \\ &\boldsymbol{\Gamma}_D = [\boldsymbol{d}_\tau^{\mathrm{T}}, \boldsymbol{d}_f^{\mathrm{T}}]^{\mathrm{T}} \in \mathbb{R}^6, \ \boldsymbol{\Gamma}_c = [\boldsymbol{u}_c^{\mathrm{T}}, \boldsymbol{f}_c^{\mathrm{T}}]^{\mathrm{T}} \in \mathbb{R}^6, \end{aligned} \tag{4}$$

where m and $\boldsymbol{J} \in \mathbb{R}^{3\times3}$ denote the mass and the symmetric positive-definite inertia matrix. $\boldsymbol{M}_g \in \mathbb{R}^3$ and $\boldsymbol{F}_g \in \mathbb{R}^3$ are the gravity-gradient moment and the gravity force on the spacecraft. $\boldsymbol{d}_\tau \in \mathbb{R}^3$ and $\boldsymbol{d}_f \in \mathbb{R}^3$ are the external disturbance torque and force. $\boldsymbol{u}_c \in \mathbb{R}^3$ and $\boldsymbol{f}_c \in \mathbb{R}^3$ denote the control torque and force. The adjoint operator $\mathrm{ad}_{\boldsymbol{\xi}}$ and the co-adjoint operator $\mathrm{ad}^*_{\boldsymbol{\xi}}$ of $\boldsymbol{\xi}$ are expressed as

$$\mathrm{ad}_{\boldsymbol{\xi}} = \begin{bmatrix} \boldsymbol{\omega}^{\times} & \boldsymbol{0}_{3\times3} \\ \boldsymbol{v}^{\times} & \boldsymbol{\omega}^{\times} \end{bmatrix}, \quad \mathrm{ad}^*_{\boldsymbol{\xi}} = \mathrm{ad}^{\mathrm{T}}_{\boldsymbol{\xi}} = \begin{bmatrix} -\boldsymbol{\omega}^{\times} & -\boldsymbol{v}^{\times} \\ \boldsymbol{0}_{3\times3} & -\boldsymbol{\omega}^{\times} \end{bmatrix}. \tag{5}$$

Considering the J_2 perturbation of the Earth's oblateness and the coupling between translational and rotational motion, $\boldsymbol{M}_g$ and $\boldsymbol{F}_g$ in the body-fixed frame $\mathcal{B}$ are expressed as (Lee & Vukovich, 2016, Eqs. (5)–(7)). We assume that a virtual leader spacecraft flies in the absence of external disturbances and control. The subscript d indicates that the parameter is related to the virtual leader spacecraft. Thus, the virtual leader spacecraft is expressed as

$$\begin{cases} \dot{\boldsymbol{g}}_d = \boldsymbol{g}_d\hat{\boldsymbol{\xi}}_d, \\ \boldsymbol{\Xi}_d\dot{\boldsymbol{\xi}}_d = \mathrm{ad}^*_{\boldsymbol{\xi}_d}\boldsymbol{\Xi}_d\boldsymbol{\xi}_d + \boldsymbol{\Gamma}_{gd}(\boldsymbol{\Xi}_d), \end{cases} \tag{6}$$

where the definitions of parameters are similar to (2) and (3). When the initial orbit and attitude parameters of the virtual leader spacecraft are known, (6) produces a desired tracking pose for the controllable spacecraft.

2.2. Relative kinematics and dynamics of a spacecraft on SE(3) under input saturation

Let $\boldsymbol{g}_e \in \mathbb{R}^{4\times4}$ denotes the relative error between the pose of the virtual leader spacecraft and the pose of the controllable spacecraft, can be expressed as (Mei et al., 2022)

$$\boldsymbol{g}_e = \boldsymbol{g}_d^{-1}\boldsymbol{g} = \begin{bmatrix} \boldsymbol{R}_d^{\mathrm{T}}\boldsymbol{R} & \boldsymbol{R}_d^{\mathrm{T}}(\boldsymbol{p} - \boldsymbol{p}_d) \\ 0_{1\times3} & 1 \end{bmatrix} = \begin{bmatrix} \boldsymbol{R}_e & \boldsymbol{p}_e \\ \boldsymbol{0}_{1\times3} & 1 \end{bmatrix}. \tag{7}$$

Then, by the exponential coordinates, the pose configuration error $\boldsymbol{g}_e$ can be uniformly expressed as (Zhang, Biggs, Ye, & Sun, 2019)

$$\boldsymbol{\eta} = \begin{bmatrix} \boldsymbol{\Phi} \\ \boldsymbol{\Psi} \end{bmatrix} = \left[\log_{\mathrm{SE}(3)} \boldsymbol{g}_e\right]^{\vee} = \begin{bmatrix} \boldsymbol{\Phi}^{\times} & \boldsymbol{\Psi} \\ \boldsymbol{0}_{1\times3} & 0 \end{bmatrix}^{\vee} \in \mathbb{R}^6, \tag{8}$$

where $[\cdot]^{\vee}$ is the operation of mapping the Lie algebra to the corresponding vector. $\boldsymbol{\Phi} \in \mathbb{R}^3$ and $\boldsymbol{\Psi} \in \mathbb{R}^3$ are the attitude and the position tracking error, respectively, which are expanded as Zhang, Biggs, et al. (2019, Eq. (15) and Eq. (16)).

The relative velocity error $\boldsymbol{\xi}_e = [\boldsymbol{\omega}_e^{\mathrm{T}}, \boldsymbol{v}_e^{\mathrm{T}}]^{\mathrm{T}} \in \mathbb{R}^6$ in the body-fixed frame $\mathcal{B}$ of the controllable spacecraft is (Lee, Sanyal, & Butcher, 2015)

$$\boldsymbol{\xi}_e = \boldsymbol{\xi} - \mathrm{Ad}_{\boldsymbol{g}_e^{-1}}\boldsymbol{\xi}_d. \tag{9}$$

In addition, the adjoint matrix mapping operation of the Lie group SE(3) is introduced as Zhang, Biggs, et al. (2019, Eq. (18)).

Then, the relative kinematics of a spacecraft using exponential coordinates can be represented as

$$\dot{\boldsymbol{\eta}} = \boldsymbol{G}(\boldsymbol{\eta})\boldsymbol{\xi}_e, \tag{10}$$

where the definitions of $\boldsymbol{G}(\boldsymbol{\eta})$ is expressed in Zhang, Biggs, et al. (2019, Eq. (20a)). Then, taking the dynamics (3) into the time derivative of (9) and using the fact in Lee and Vukovich (2016, Appendix), the relative dynamics of the spacecraft are expressed as

$$\dot{\boldsymbol{\xi}}_e = \boldsymbol{H} + \boldsymbol{\Xi}^{-1}\boldsymbol{\Gamma}_c + \boldsymbol{\Xi}^{-1}\boldsymbol{\Gamma}_g(\boldsymbol{\Xi}) + \boldsymbol{\Gamma}_D, \tag{11}$$

where $\boldsymbol{H} = \boldsymbol{\Xi}^{-1}\,\mathrm{ad}^*_{\boldsymbol{\xi}}\,\boldsymbol{\Xi}\boldsymbol{\xi} + \mathrm{ad}_{\boldsymbol{\xi}_e}\,\mathrm{Ad}_{\boldsymbol{g}_e^{-1}}\,\boldsymbol{\xi}_d - \mathrm{Ad}_{\boldsymbol{g}_e^{-1}}\,\dot{\boldsymbol{\xi}}_d$.

Assumption 1. The unknown disturbance $\boldsymbol{\Gamma}_D$ of the spacecraft is bounded by an unknown positive constant $D_{\max}$, i.e., $\|\boldsymbol{\Gamma}_D\| \le D_{\max}$.

In addition, the actuator saturation is also considered. The saturated control input $\boldsymbol{\Gamma}_c = [\Gamma_{c,1}, \ldots, \Gamma_{c,6}]^{\mathrm{T}} \in \mathbb{R}^6$ in (11) is defined as $\boldsymbol{\Gamma}_{c,i} = \mathrm{sign}(U_{c,i})\min(U_{\mathrm{sat},c,i}, |U_{c,i}|)$ (Kang et al., 2023), where $U_{c,i}$ and $U_{\mathrm{sat},c,i}$ are the nominal input and saturation limit of the ith actuator of the spacecraft with $i = 1, \ldots, 6$. The nonlinear saturation $\boldsymbol{\Gamma}_c$ in this work is approximately modeled as $\bar{\boldsymbol{\Gamma}}_c = [\bar{\boldsymbol{u}}_c^{\mathrm{T}}, \bar{\boldsymbol{f}}_c^{\mathrm{T}}]^{\mathrm{T}} = [\bar{\Gamma}_{c,1}, \ldots, \bar{\Gamma}_{c,6}]^{\mathrm{T}} \in \mathbb{R}^6$ by using a dead-zone based model (Mousavi & Khayatian, 2011; Yue et al., 2023) with the relation

$$\bar{\Gamma}_{c,i} = \rho_{0,c,i}U_{c,i} - \int_0^{K_{c,i}} \rho_{c,i}(k)\mathcal{Z}(k, U_{c,i})dk, \tag{12}$$

where $\rho_{c,i}(k)$ is a known density function and is given as $\rho_{c,i}(k) = \begin{cases} \frac{2}{K_{c,i}} & r \le K_{c,i}, \\ 0 & r > K_{c,i}, \end{cases}$. The dead-zone operator $\mathcal{Z}(k, U_{c,i})$ is defined as $\mathcal{Z}(k, u_{c,i}) = \max\big(U_{c,i} - k, \min(0, U_{c,i} + k)\big)$. Meanwhile, $\rho_{0,c,i} = \int_0^{K_{c,i}} \rho_{c,i}(k)dk$ is a positive known constant parameter. According to Kang et al. (2023, Eq. (9)), we further have $U_{\mathrm{sat},c,i} = K_{c,i}$ from $\rho_{c,i}(k)$.

Then, the relative dynamics (11) can be rewritten as

$$\dot{\boldsymbol{\xi}}_e = \boldsymbol{H} + \boldsymbol{\Xi}^{-1}\bar{\boldsymbol{\Gamma}}_c + \boldsymbol{\Xi}^{-1}\boldsymbol{\Gamma}_g(\boldsymbol{\Xi}) + \boldsymbol{\Gamma}_D, \tag{13}$$

with $\bar{\boldsymbol{\Gamma}}_c = \boldsymbol{\rho}_{0,c} \circ \boldsymbol{U}_c - \boldsymbol{L}_c$,

where $\boldsymbol{\rho}_{0,c} = [\rho_{0,c,1}, \ldots, \rho_{0,c,6}]^{\mathrm{T}} \in \mathbb{R}^6$, $\boldsymbol{L}_c = [l_{c,1}, \ldots, l_{c,6}]^{\mathrm{T}} \in \mathbb{R}^6$ with $l_{c,i} = \int_0^{K_{c,i}} \rho_{c,i}(k)\mathcal{Z}(k, U_{c,i})dk$, $i = 1, \ldots, 6$. $\boldsymbol{U}_c = [U_{c,1}, \ldots, U_{c,6}]^{\mathrm{T}} \in \mathbb{R}^6$ represents the controller output to be designed and the symbol $\circ$ denotes Hadamard product (Horn, 1990).

2.3. Attitude and obstacle-avoidance constraints

In this subsection, the models of attitude constraints and obstacle-avoidance constraints are given.

2.3.1. Attitude constraint

As shown in Fig. 2(a), for the spacecraft, $\boldsymbol{a}_m$ is the center-pointing unit vector in the body-fixed frame $\mathcal{B}$ of the mth ($m = 1, 2, \ldots, M$) sensitive spaceborne equipment. There are N bright objects corresponding to the mth sensitive spaceborne equipment, which is located at position $\boldsymbol{p}_n \in \mathbb{R}^3$ ($n = 1, 2, \ldots, N$) in the ECI frame $\mathcal{I}$. The half cone angle of the field of view of the mth sensitive spaceborne equipment to the nth bright object is represented by θ_m^n ($0 < \theta_m^n < \pi$).

In this work, when $\|\boldsymbol{p}_n\| \ge 100\|\boldsymbol{p}\|$ is satisfied, the relative motion between the bright object and the spacecraft can be ignored. The corresponding attitude-forbidden zone is defined as the static attitude-forbidden zone (SAFZ). When another kind

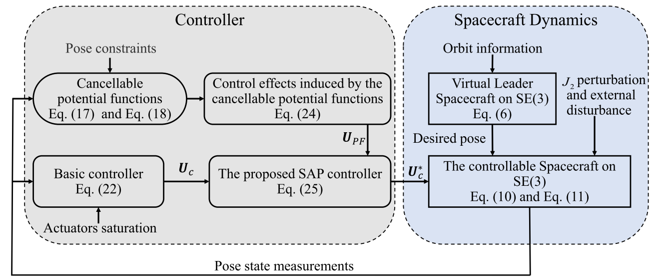

Fig. 1. Diagram of saturated adaptive pose control system.

of bright object is close to the spacecraft, the relative motion between them cannot be ignored. The corresponding attitude-forbidden zone is defined as the dynamic attitude-forbidden zone (DAFZ). Then, the static/dynamic attitude-forbidden zone of the mth sensitive spaceborne equipment and the nth bright object can be uniformly expressed as

$$\boldsymbol{a}_m^T \boldsymbol{R}^T \boldsymbol{l}_n < \cos(\theta_m^n), \tag{14}$$

$$\text{with } \boldsymbol{l}_n = \begin{cases} \frac{\boldsymbol{p}_n}{\|\boldsymbol{p}_n\|}, & \text{if } \|\boldsymbol{p}_n\| \ge 100\|\boldsymbol{p}\|, \\ \frac{\boldsymbol{p}_n - \boldsymbol{p}}{\|\boldsymbol{p}_n - \boldsymbol{p}\|}, & \text{otherwise.} \end{cases} \tag{15}$$

In this work, the SAFZ is for distant bright objects (e.g., the Sun). The DAFZ is for neighboring bright objects (e.g., flames generated by multiple engines of adjacent non-cooperative spacecraft). We also assume that all luminous objects are considered to be bright spheres.

2.3.2. Obstacle-avoidance constraint

In this work, obstacle-avoidance between the spacecraft and Q space obstacles (space debris or non-cooperative neighbor spacecraft) is considered. Assuming that the positions of all space obstacles are known, the qth space obstacle is located at position $\boldsymbol{p}_q \in \mathbb{R}^3$ in the ECI frame $\mathcal{I}$. The collision constraint of the spacecraft and the qth space obstacle is expressed as

$$d_s^q = \|\boldsymbol{p} - \boldsymbol{p}_q\| > d_q, \quad q = 1, 2, \ldots, Q, \tag{16}$$

where d_q represents the minimum distance between the spacecraft and the qth obstacle. d_s^q is the relative distance between the spacecraft and the qth obstacle.

Assumption 2. The desired pose $\boldsymbol{g}_d$ from the virtual leader spacecraft and the initial pose $\boldsymbol{g}(t = 0)$ of the spacecraft meet the mixed attitude constraints (14) and obstacle-avoidance constraints (16).

3. Problem statement

The objective of this paper is to design a SAP controller for the spacecraft on SE(3) to achieve the desired pose configuration $\boldsymbol{g}_d$ tracking in the presence of attitude constraints and obstacle-avoidance constraints, input saturation, and disturbances, as shown in Fig. 1.

This work mainly solves the following two problems:

Problem 1 (*Cancellable Potential Function*)**.** Considering the constraints composed of multiple static/dynamic attitude-forbidden zones and multiple space obstacles, propose cancellable potential functions that can disappear at the desired pose configuration $\boldsymbol{g}_d$.

Problem 2 (*Saturated Adaptive Pose Controller*)**.** Based on the uniformly asymptotically stable theory of nonlinear vanishing perturbation systems, design an SAP controller leveraging the cancellable potential function to achieve the desired pose configuration $\boldsymbol{g}_d$ tracking under the multiple constraints.

4. Cancellable potential function

In this section, we solve Problem 1. Suppose the spacecraft is with M sensitive spaceborne instruments, and there are N_1 bright objects (at long distance) corresponding to the mth ($m = 1, 2, \ldots, M$) equipment. Meanwhile, there are Q space obstacles around the orbit of the virtual leader spacecraft, and each space obstacle is assumed to be a bright object at a close distance.

4.1. Attitude cancellable potential function

There are M sensitive spaceborne instruments, which is required to avoid exploring directly to both N_1 bright objects at long distance and Q space obstacles at close distance. Therefore, there are $N = N_1 + Q$ static/dynamic attitude-forbidden zones for the mth ($m = 1, 2, \ldots, M$) equipment. To further protect the sensitive equipment, we define an warning angle σ_m^n ($\theta_m^n < \sigma_m^n < \pi$) for the nth ($n = 1, 2, \ldots, N$) attitude-forbidden zone.

Assumption 3. The desired pose configuration $\boldsymbol{g}_d$ makes the center pointing vector of the mth sensitive spaceborne equipment outside the nth bright object attitude warning zone, i.e., $\langle \boldsymbol{a}_m, \boldsymbol{R}_d^{\mathrm{T}}\boldsymbol{l}_n\rangle > \sigma_m^n$, where $\langle \boldsymbol{a}, \boldsymbol{b}\rangle$ is the angle of vectors $\boldsymbol{a}$ and $\boldsymbol{b}$.

Then, motivated by Kang, Shen, and Wu (2020, Definition 2) and based on attitude constraint model (14) and Assumption 3, the attitude cancellable potential function U_m^n is constructed as

$$U_m^n = \begin{cases} \dfrac{\left(\boldsymbol{a}_m^{\mathrm{T}}\boldsymbol{R}^{\mathrm{T}}\boldsymbol{l}_n - \cos(\sigma_m^n)\right)^2}{\left(\cos(\theta_m^n) - \boldsymbol{a}_m^{\mathrm{T}}\boldsymbol{R}^{\mathrm{T}}\boldsymbol{l}_n\right)^2}, & \theta_m^n < \langle \boldsymbol{a}_m, \boldsymbol{R}^{\mathrm{T}}\boldsymbol{l}_n\rangle \le \sigma_m^n, \\ 0, & \sigma_m^n < \langle \boldsymbol{a}_m, \boldsymbol{R}^{\mathrm{T}}\boldsymbol{l}_n\rangle, \end{cases} \tag{17}$$

where $m = 1, \ldots, M$, $n = 1, \ldots, N$. σ_m^n is the nth warning angle of the mth sensitive equipment.

As observed in (17), the attitude cancellable potential function U_m^n works only when the mth sensitive spaceborne equipment center pointing vector $\boldsymbol{a}_m$ is located in the warning zone of the nth attitude-forbidden zone.

4.2. Obstacle-avoidance cancellable potential function

Suppose that the qth ($q = 1, 2, \ldots, Q$) space obstacle and the spacecraft are in the spherical envelope with radii r_q and r_s, respectively, as shown in Fig. 2(b). Thus, the minimum distance $d_q = r_q + r_s$ in (16) between the spacecraft and the qth space obstacle. Then, we define the warning distance d_w^q ($d_w^q > d_q$) for the spacecraft.

Definition 1. [Warning distance] As shown in Fig. 2(b), suppose that the spacecraft with mass m is approaching the qth space obstacle with its maximum allowable relative speed $v_{\max}$. The initial relative position of the qth space obstacle to the spacecraft is $d_{s,0}^q$. If the maximum force $f_{c,\max}$ is applied to decelerate the spacecraft, the final relative speed of the spacecraft reduces to zero when the relative distance of the qth space obstacle and the spacecraft is $d_{s,t}^q = d_q$. The warning distance of the spacecraft and the qth space obstacle is $d_w^q = d_{s,0}^q - d_{s,t}^q + d_q = d_{s,0}^q$. Then, the spherical zone with the warning distance d_w^q as the radius is regarded as the collision warning zone between the spacecraft and the qth space obstacle.

According to Definition 1, we have $d_q = \frac{1}{2}\frac{f_{\max}}{m}t^2 - v_{\max}t + d_w^q$. Then, we can obtain a unique solution to t as well. Thus, the warning distance d_w^q can be defined as $d_w^q = \frac{1}{2}\frac{m}{f_{\max}}v_{\max}^2 + d_q$.

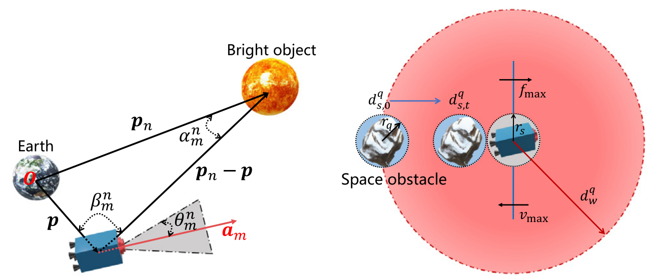

(a) Attitude constraint (b) Obstacle-avoidance constraint

Fig. 2. Schematic diagram of pose constraints.

Assumption 4. The desired pose configuration $\boldsymbol{g}_d$ makes the qth space obstacle outside the qth collision warning zone of the spacecraft, i.e., $\|\boldsymbol{p}_d - \boldsymbol{p}_q\| > d_w^q$.

Then, according to the obstacle-avoidance constraint model (16) and Assumption 4, the obstacle-avoidance cancellable potential function F_q is given as

$$F_q = \begin{cases} \dfrac{\left((d_w^q)^2 - \|\boldsymbol{p} - \boldsymbol{p}_q\|^2\right)^2}{\left(\|\boldsymbol{p} - \boldsymbol{p}_q\|^2 - d_q^2\right)^2}, & d_q < \|\boldsymbol{p} - \boldsymbol{p}_q\| \le d_w^q, \\ 0, & d_w^q < \|\boldsymbol{p} - \boldsymbol{p}_q\|. \end{cases} \tag{18}$$

The obstacle-avoidance cancellable potential function F_q is only effective when the qth space obstacle enters the qth collision warning zone of the spacecraft.

From (17) and (18), the desired pose configuration $\boldsymbol{g}_d$ is the equilibrium point of the attitude cancellable potential function U_m^n and the obstacle-avoidance cancellable potential function F_q. To this end, this kind of potential function is defined as a cancellable potential function.

5. Saturated adaptive pose controller

In this section, we solve Problem 2. In order to design the controller, a sliding mode vector $\boldsymbol{s} \in \mathbb{R}^6$ is constructed as $\boldsymbol{s} = \boldsymbol{\xi}_e + \mathcal{V}_1\boldsymbol{\eta}$, where $\mathcal{V}_1 = \mathrm{diag}(\nu_{11}, \ldots, \nu_{16}) \in \mathbb{R}^{6\times 6}$ is positive-definite diagonal matrix with positive diagonal elements. According to (10) and (13) of the spacecraft, the time derivative of $\boldsymbol{s}$ is

$$\dot{\boldsymbol{s}} = \boldsymbol{H} + \boldsymbol{\varXi}^{-1}\bar{\boldsymbol{\Gamma}}_c + \boldsymbol{\varXi}^{-1}\boldsymbol{\Gamma}_g(\boldsymbol{\varXi}) + \boldsymbol{\Gamma}_D + \mathcal{V}_1\boldsymbol{G}(\boldsymbol{\eta})\boldsymbol{\xi}_e. \tag{19}$$

Noted that the upper bound $D_{\max}$ of the disturbances $\boldsymbol{\Gamma}_D$ is limited by a known constant, thus the estimation $\hat{D}_{\max}$ of the parameter $D_{\max}$ is also limited to a known bounded convex set. This can be realized by using a smooth projection algorithm (Thakur, Srikant, & Akella, 2015) to modify the parameter update law. Two convex sets are defined as

$$\begin{aligned} \varOmega_{D_{\max}} &\triangleq \left\{D_{\max} \in \mathbb{R} \mid D_{\max}^2 < \epsilon\right\} \\ \varOmega_{\hat{D}_{\max}} &\triangleq \left\{\hat{D}_{\max} \in \mathbb{R} \mid \hat{D}_{\max}^2 < \epsilon + \delta\right\} \end{aligned} \tag{20}$$

where $\epsilon > 0$ and $\delta > 0$ are known constants. The smooth projection-based update law for $\hat{D}_{\max}$ is given by

$$\dot{\hat{D}}_{\max} = \mathrm{Proj}\left(\hat{D}_{\max}, \varUpsilon\right), \quad \varUpsilon \triangleq \lambda_{\max}(\boldsymbol{\varXi})\|\boldsymbol{s}\|, \tag{21}$$

where $\mathrm{Proj}\left(\hat{D}_{\max}, \varUpsilon\right) \triangleq$

$$\begin{cases} \beta\varUpsilon & \text{if } \hat{D}_{\max}^2 < \epsilon \\ \beta\left(\varUpsilon - \dfrac{\left(\hat{D}_{\max}^2 - \epsilon\right)\varUpsilon\hat{D}_{\max}}{\delta\hat{D}_{\max}^2}\hat{D}_{\max}\right) & \text{if } \hat{D}_{\max}^2 \ge \epsilon \end{cases}$$

with β being a positive constant.

Then, according to (19) and the projection-based update law for $\hat{D}_{\max}$ in (21), a basic controller is designed as

$$\boldsymbol{U}_c = \boldsymbol{\chi}\circ\Big(-\boldsymbol{\Xi}(\boldsymbol{H}+\mathcal{V}_1\boldsymbol{G}(\boldsymbol{\eta})\boldsymbol{\xi}_e)-\boldsymbol{\Gamma}_g(\boldsymbol{\Xi}) - \boldsymbol{k}_1\boldsymbol{s} - \frac{\lambda_{\max}(\boldsymbol{\Xi})\hat{D}_{\max}\boldsymbol{s}}{\|\boldsymbol{s}\|+\kappa^2} + \boldsymbol{L}_c\Big), \tag{22}$$

where $\boldsymbol{k}_1 = \mathrm{diag}(k_{11},\ldots,k_{16}) \in \mathbb{R}^{6\times 6}$ is a positive-definite diagonal matrix, $\boldsymbol{\chi} = [\frac{1}{\rho_{0,c,1}},\ldots,\frac{1}{\rho_{0,c,6}}]^{\mathrm{T}} \in \mathbb{R}^6$, and the updating laws for the adaptive parameter κ is proposed as $\dot{\kappa} = -\frac{k_2\lambda_{\max}(\boldsymbol{\Xi})\kappa\|\boldsymbol{s}\|}{\|\boldsymbol{s}\|+\kappa^2}\hat{D}_{\max}$.

Using the proposed basic controller $\boldsymbol{U}_c$ in (22), we have the following theorem.

Theorem 1. *For the spacecraft expressed by* (10) and (13), *the proposed basic controller* (22) *ensures that* $\lim_{t\to\infty}\boldsymbol{\eta}(t) = \boldsymbol{0}$ *and* $\lim_{t\to\infty}\boldsymbol{\xi}_e(t) = \boldsymbol{0}$.

Proof. Consider the Lyapunov function $V_1 = \frac{1}{2}\boldsymbol{s}^{\mathrm{T}}\boldsymbol{\Xi}\boldsymbol{s} + V_{D_{\max}} + V_{\kappa}$, where $V_{D_{\max}} = \frac{1}{2\beta}\tilde{D}^2_{\max}$ and $V_\kappa = \frac{1}{2k_2}\kappa^2$ with $\tilde{D}_{\max} = D_{\max} - \hat{D}_{\max}$.

Substituting (19) and the proposed basic controller (22) into the time derivative of V_1 yields

$$\begin{aligned}\dot{V}_1 \le& -\min(\boldsymbol{k}_1)\boldsymbol{s}^{\mathrm{T}}\boldsymbol{s} - \lambda_{\max}(\boldsymbol{\Xi})\|\boldsymbol{s}\|\hat{D}_{\max} \\ &+ \lambda_{\max}(\boldsymbol{\Xi})\|\boldsymbol{s}\|D_{\max} - \frac{1}{\beta}\tilde{D}_{\max}\dot{\hat{D}}_{\max} \\ \le& -\min(\boldsymbol{k}_1)\boldsymbol{s}^{\mathrm{T}}\boldsymbol{s} - \mathcal{C},\end{aligned} \tag{23}$$

where $\mathcal{C} = -\frac{1}{\beta}\tilde{D}_{\max}(\dot{\hat{D}}_{\max} - \beta\lambda_{\max}(\boldsymbol{\Xi})\|\boldsymbol{s}\|)$ and $\min(\cdot)$ is the minimum element.

According to (21), $\mathcal{C} = 0$ if $\hat{D}^2_{\max} < \epsilon$. In addition, when $\hat{D}^2_{\max} \ge \epsilon$, $\mathcal{C} = \frac{(\hat{D}^2_{\max}-\epsilon)\Upsilon\hat{D}_{\max}}{\delta\hat{D}^2_{\max}}\tilde{D}_{\max}\hat{D}_{\max} \le 0$ due to $\tilde{D}_{\max}\hat{D}_{\max} = D_{\max}\hat{D}_{\max} - \hat{D}^2_{\max} \le 0$ when $\hat{D}^2_{\max} \ge \epsilon$. Therefore, $\dot{V}_1 \le -\min(\boldsymbol{k}_1)\boldsymbol{s}^{\mathrm{T}}\boldsymbol{s}$, since $\min(\boldsymbol{k}_1) > 0$. By invoking Barbalat's Lemma (Khalil, 2002, Section 8.3), it yields that $\lim_{t\to\infty}\boldsymbol{s}(t) = \boldsymbol{0}$. Then, consider the Lyapunov function $V_2 = \frac{1}{2}\boldsymbol{\eta}^{\mathrm{T}}\boldsymbol{\eta}$, substituting (10) and $\boldsymbol{\xi}_e = -\mathcal{V}_1\boldsymbol{\eta}$ into the time derivative of V_2 further yields $\dot{V}_2 = -\mathcal{V}_1\boldsymbol{\eta}^{\mathrm{T}}\boldsymbol{G}(\boldsymbol{\eta})\boldsymbol{\eta} \le -\lambda_{\min}(\mathcal{V}_1)\boldsymbol{\eta}^{\mathrm{T}}\boldsymbol{\eta}$, where the fact $\boldsymbol{G}(\boldsymbol{\eta})\boldsymbol{\eta} = \boldsymbol{\eta}$ (Lee et al., 2015) is used. Then, based on Barbalat's Lemma, the pose error $\boldsymbol{\eta} = \boldsymbol{0}$ as $t \to \infty$. When $\boldsymbol{\eta} = \boldsymbol{0}$, we can get $\dot{\boldsymbol{\eta}} = \boldsymbol{0}$, and then substitute it into (10) to further obtain $\boldsymbol{\xi}_e = \boldsymbol{0}$ due to $\boldsymbol{G}(\boldsymbol{\eta}) \ne \boldsymbol{0}$. Thus, it is clear that $\lim_{t\to\infty}\boldsymbol{\eta}(t) = \boldsymbol{0}$ and $\lim_{t\to\infty}\boldsymbol{\xi}_e(t) = \boldsymbol{0}$.

This completes the proof. ■

Then, the force and torque produced by the cancellable potential functions (17) and (18) can be expressed as

$$\boldsymbol{U}_{PF} = \left[-k_3\sum_{m=1}^{M}\sum_{n=1}^{N}\frac{\partial U^n_m}{\partial(\boldsymbol{R}\boldsymbol{a}_m)}, -k_4\boldsymbol{R}^{\mathrm{T}}\sum_{q=1}^{Q}\frac{\partial F_q}{\partial \boldsymbol{p}}\right]^{\mathrm{T}}. \tag{24}$$

Then, the SAP controller is designed as

$$\boldsymbol{U}^*_c = \bar{\boldsymbol{U}}_c + \boldsymbol{\chi}\circ\bar{\boldsymbol{U}}_{PF}, \tag{25}$$

where $\bar{\boldsymbol{U}}_c = \boldsymbol{\rho}^*_{0,c}\circ\boldsymbol{U}_c - \boldsymbol{L}^*_c \in \mathbb{R}^6$, the ith actuator saturation value $K^*_{c,i} = K_{c,i}$, and $\bar{\boldsymbol{U}}_{PF} = \boldsymbol{\rho}_{0,PF}\circ\boldsymbol{U}_{PF} - \boldsymbol{L}_{PF} \in \mathbb{R}^6$ is the dead-zone based saturation operation for the control force/torque (24).

In this work, we assume that the saturated value $K_{PF,i} = 4K_{c,i}$ is given. This setting is for $\|\bar{\boldsymbol{U}}_c\| < \|\boldsymbol{\chi}\circ\bar{\boldsymbol{U}}_{PF}\|$ to achieve that the potential function plays a leading role when it is necessary to ensure the safety of the spacecraft. The selection $K_{PF,i} = 4K_{c,i}$ is not unique, and suitable coefficients can be determined through multiple simulations.

Then, the SAP controller (25) is substituted into the time derivative of (19) to further obtain

$$\dot{\boldsymbol{s}} = f(t,\boldsymbol{s}) + h(t,\boldsymbol{s}), \tag{26}$$

where $f(t,\boldsymbol{s})$ and $h(t,\boldsymbol{s}) = \boldsymbol{\Xi}^{-1}\bar{\boldsymbol{U}}_{PF}$ represent the nominal system and the perturbation term, respectively, and

$$f(t,\boldsymbol{s}) = \boldsymbol{H} + \boldsymbol{\Xi}^{-1}(\boldsymbol{\rho}_{0,c}\circ\boldsymbol{U}_c - \boldsymbol{L}_c) + \boldsymbol{\Xi}^{-1}\boldsymbol{\Gamma}_g(\boldsymbol{\Xi})$$

where $\boldsymbol{\rho}_{0,c}\circ\bar{\boldsymbol{U}}_c - \boldsymbol{L}_c = \boldsymbol{\rho}_{0,c}\circ\boldsymbol{U}_c - \boldsymbol{L}_c$ is applied.

According to Theorem 1, when $\lim_{t\to\infty}\boldsymbol{s}(t) = \boldsymbol{0}$, the spacecraft reaches the equilibrium point. At this time, according to (17) and (18), the perturbation term $h(t,\boldsymbol{0}) = \boldsymbol{0}$. Therefore, the system (26) is a vanishing perturbation system. Thus, the stability of the vanishing perturbation system (26) is summarized as

Theorem 2. *When the positive vector $\boldsymbol{k}_1$ is selected to be sufficiently large, the origin $\boldsymbol{s} = \boldsymbol{0}$ is a uniformly asymptotically equilibrium point of the perturbed system* (26).

Proof. By choosing the same Lyapunov function V_1 as in Theorem 1, we obtained $\frac{\partial V_1}{\partial t} + \frac{\partial V_1}{\partial \boldsymbol{s}}f(t,\boldsymbol{s}) \le -\min(\boldsymbol{k}_1)\|\boldsymbol{s}\|^2$, and $\left\|\frac{\partial V_1}{\partial \boldsymbol{s}}\right\| \le \lambda_{\max}(\boldsymbol{\Xi})\|\boldsymbol{s}\|$ by following the same procedures as in Theorem 1.

Then, the derivative of V_1 along the trajectories of (26) is given by $\dot{V}_1 \le -\min(\boldsymbol{k}_1)\|\boldsymbol{s}\|^2 + \lambda_{\max}(\boldsymbol{\Xi})\|\boldsymbol{s}\|\|h(t,\boldsymbol{s})\|$. If the perturbation term $h(t,\boldsymbol{s})$ satisfies

$$\|h(t,\boldsymbol{s})\| \le \gamma\|\boldsymbol{s}\|, \quad \gamma < \frac{\min(\boldsymbol{k}_1)}{\lambda_{\max}(\boldsymbol{\Xi})}, \tag{27}$$

then according to the uniformly asymptotically stable theory of nonlinear vanishing perturbation systems in Khalil (2002, Section 9.1), the origin $\boldsymbol{s} = 0$ is a uniformly asymptotically stable equilibrium point of the perturbed system (26). Thus, the proof can be completed by showing (27) is established. It can be proved in three cases:

1. When $\boldsymbol{s} = \boldsymbol{0}$, $h(t,\boldsymbol{s}) = \boldsymbol{0}$, the spacecraft at the equilibrium point, it is obvious that (27) is established.
2. When $\boldsymbol{s} \ne \boldsymbol{0}$, $h(t,\boldsymbol{s}) = \boldsymbol{0}$, the spacecraft is outside any attitude/collision warning zone. It is obvious that (27) is established.
3. When $\boldsymbol{s} \ne \boldsymbol{0}$, $h(t,\boldsymbol{s}) \ne \boldsymbol{0}$, the spacecraft are within one or more attitude/collision warning zones. In view of 1, we can get $\|h(t,\boldsymbol{s})\| \le \lambda_{\max}(\boldsymbol{\Xi}^{-1})\|\bar{\boldsymbol{U}}_{PF}\|$. Since $\lambda_{\max}(\boldsymbol{\Xi}^{-1})$ and $\|\boldsymbol{U}_{\mathrm{sat},c}\|$ are known, $\|\bar{\boldsymbol{U}}_{PF}\|$ is a bounded value. Therefore, when the inertial parameters $\boldsymbol{\Xi}$ of the spacecraft are determined, the larger the minimum element of the vector $\boldsymbol{k}_1$, the more conducive to the establishment of (27).

This completes the proof. ■

Then, based on Theorem 2, the sliding mode vector satisfies $\lim_{t\to\infty}\boldsymbol{s}(t) = \boldsymbol{0}$. From Theorem 1, we further get $\lim_{t\to\infty}\boldsymbol{\eta}(t) = \boldsymbol{0}$ and $\lim_{t\to\infty}\boldsymbol{\xi}_e(t) = \boldsymbol{0}$. Therefore, the SAP controller achieves tracking of the desired pose configuration $\boldsymbol{g}_d$ despite multiple constraints.

Remark 1. Recalling the following previous works:

1. In Huang, Yan, and Zhou (2017, Theorem 2, Eq. (59)), it is not strict to directly assume that inequality (27) is satisfied.
2. In Huang, Yan, Zhou, and Yang (2017, Theorem 1, Eq. (69)) and Zhang, Ye, et al. (2019, Theorem 2, Eq. (39)), the potential function in the inequality of the perturbation term and the equilibrium point tends to infinity, thus it is difficult to find the proper parameters that satisfy the inequality relation.

In this work, after introducing the saturation operation, the term $\|h(t,\boldsymbol{s})\|$ is bounded rather than tending to infinity in the aforementioned works. Based on this, we obtain conservative conditions for the establishment of inequality (27), which is a major contribution of this work.

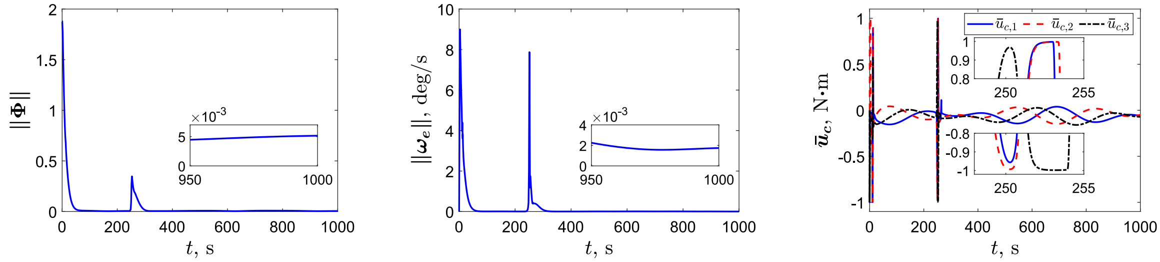

(a) Attitude error (b) Angular velocity error (c) Saturation control torque

Fig. 3. The time history of the quantity related to attitude state of the spacecraft under the proposed controller (25).

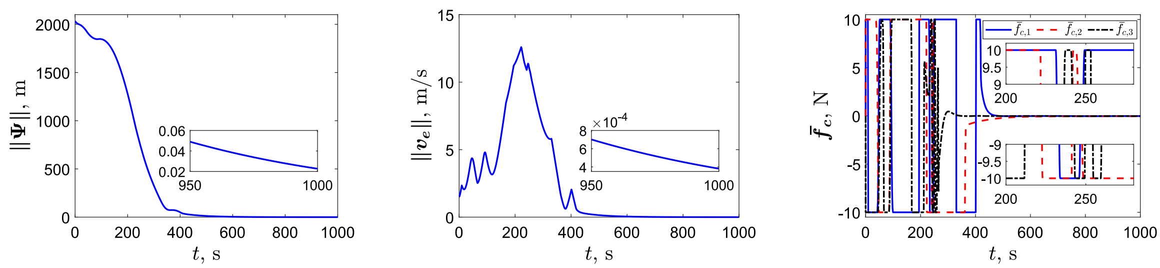

(a) Position error (b) Translational velocity error (c) Saturation control force

Fig. 4. The time history of the quantity related to position state of the spacecraft under the proposed controller (25).

Remark 2. According to the adaptive law (21), a larger β may cause oscillations, while a smaller β may slow down the stabilization speed of the adaptive parameter $\mathrm{Proj}\big(\hat{D}_{\max}, \Upsilon\big)$. Moreover, for parameters in basic controller (22), a larger $\boldsymbol{k}_1$ may lead to excessive system damping and slower convergence speed, whereas a smaller $\boldsymbol{k}_1$ may cause unnecessary oscillations. Meanwhile, a larger $\boldsymbol{k}_1\mathcal{V}_1$ may accelerate the convergence speed of the system but cause unnecessary oscillations. Finally, larger k_3 and k_4 in (24) may lead to severe oscillations when the spacecraft responds to pose constraints, while smaller k_3 and k_4 may cause violation of the pose constraints.

6. Simulation results

In this section, the effectiveness of the proposed SAP controller (25) is verified by a numerical simulation.

The Orbital Elements of the virtual leader spacecraft are provided to the same as Kang et al. (2022). The inertia parameters of the two spacecraft and the input limits of the attitude actuators and the translation actuators are set to the same as Mei et al. (2022). The initial pose configuration $\boldsymbol{g}_d(0)$ and velocity $\boldsymbol{\xi}_d(0)$ of the virtual leader spacecraft are

$$\boldsymbol{g}_d(0) = \begin{bmatrix} 0.3526 & -0.64 & 0.6827 & -1.1991\times 10^6 \\ -0.64 & 0.3674 & 0.6749 & 6.1442\times 10^6 \\ -0.6827 & -0.6749 & -0.28 & 2.8105\times 10^6 \\ 0 & 0 & 0 & 1 \end{bmatrix},$$

$$\boldsymbol{\xi}_d(0) = 10^3 \times [0, 0, 0, -2.4746, 2.1108, -6.9752]^{\mathrm{T}},$$

where the units of position vector, translation velocity vector and angular velocity vector are m, m/s and rad/s, respectively. Then, the initial attitude $\boldsymbol{R}(0)$ and the initial angular velocity $\boldsymbol{\omega}(0)$ of the spacecraft are

$$\boldsymbol{R}(0) = \begin{bmatrix} 0.5723 & -0.8138 & -0.1010 \\ 0.8138 & 0.5484 & 0.1922 \\ -0.1010 & -0.1922 & 0.9761 \end{bmatrix}, \boldsymbol{\omega}(0) = [0, 0, 0]^{\mathrm{T}}.$$

In the body-fixed frame $\mathcal{B}_d$ of the virtual leader spacecraft, the relative position and relative velocity of the spacecraft and the virtual leader spacecraft are given as $[90, -2000, 80]^{\mathrm{T}}$ m and $[1, -0.5, 1]^{\mathrm{T}}$ m/s.

The unit vector of a sensitive spaceborne equipment on the body-fixed frame $\mathcal{B}$ is $\boldsymbol{a} = [0, 0, 1]^{\mathrm{T}}$. In addition, three SAFZ in the ECI frame $\mathcal{I}$ are considered, which are the same as Kang et al. (2023, Table I). All three static forbidden angles are set to 18 deg. Three space obstacles near the orbit of the virtual leader spacecraft are considered, with relative positions $[60, -1800, 30]^{\mathrm{T}}$ m, $[25+30\sin(0.1t), -800-30\cos(0.1t), 20+30\sin(0.1t)]^{\mathrm{T}}$ m, and $[-20, -550, 600]^{\mathrm{T}}$ m. The spacecraft and three space obstacles are assumed to be within a spherical envelope with a radius of 15 m, thus $d_q = 30$ m. These three space obstacles are bright objects, forming three DAFZ with 15 deg forbidden angle. The maximum angular translation velocity of the spacecraft are $\|\boldsymbol{\omega}_e\|_{\max} = 10$ deg/s and $\|\boldsymbol{v}_e\|_{\max} = 13$ m/s. Then, the warning angle and warning distance are $\sigma_1^n = \frac{1}{2}\frac{25.5}{\|[1,1,1]\|} \times \left(\frac{10\pi}{180}\right)^2 + \theta_1^n \approx \frac{15\pi}{180} + \theta_1^n$ rad and $d_w^q = \frac{1}{2}\frac{110}{\|[10,10,10]\|} \times 13^2 + d_q \approx 530 + d_q$ m for $n = 1, 2, \ldots, 6$, θ_1^n represents the forbidden angle of each attitude-forbidden zone. For SAP controller (25), $\mathcal{V}_1 = \mathrm{diag}(0.1, 0.1, 0.1, 0.08, 0.012, 0.08)$, $\epsilon = 10^{-4}$, $\delta = 10^{-5}$, $\beta = 10^{-6}$, $D_{\max}(0) = 0$, $k_2 = 10^{-3}$, $\kappa(0) = 2$, $k_3 = 5$, $k_4 = 10^{-3}$, $\boldsymbol{k}_1 = 100\,\mathrm{diag}(1, 1, 1, 1, 1, 1)$.

As shown in Fig. 3(a), the proposed SAP controller (25) achieves attitude tracking in 350 s with a steady-state error $\|\Psi\| \leq 5\times 10^{-3}$ in 950 s. The maximum angular velocity tracking error $\|\boldsymbol{\omega}_e\|_{\max} \leq 10$ deg/s, and the steady-state error $\|\boldsymbol{\omega}_e\| \leq 3\times 10^{-3}$ deg/s in 950 s, as shown in Fig. 3(b). From Fig. 3(c), the input saturation limitation is satisfied by using the dead-zone saturation operation. From Fig. 4(a), the proposed SAP controller (25) achieves position tracking under obstacle-avoidance constraints, where the position tracking is completed in 600 s with a steady-state error $\|\Phi\| \leq 0.06$ m in 950 s. From Fig. 4(b), the maximum translation velocity tracking error is $\|\boldsymbol{v}_e\|_{\max} \leq 13$ m/s, and the translation velocity tracking error converges in 950 s with a steady-state error $\|\boldsymbol{v}_e\| \leq 8\times 10^{-4}$ m/s. From Fig. 4(c), it is clear that the saturation limit of control force is satisfied.

The angles between the pointing direction of the sensitive equipment and the central pointing of the attitude-forbidden

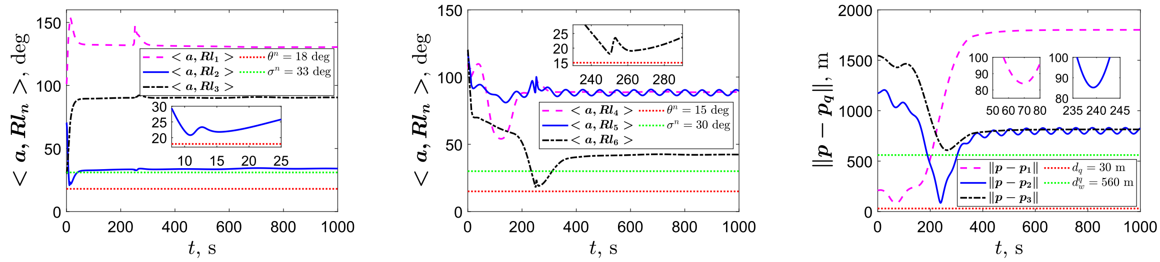

(a) Static forbidden zones (b) Dynamic forbidden zones (c) Distance from obstacles

Fig. 5. The time history of the quantity related to pose constraints of the spacecraft under the proposed controller (25).

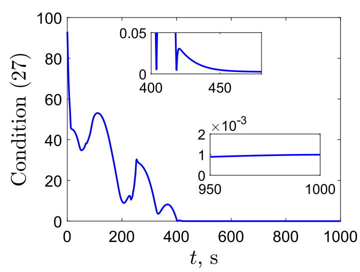

Fig. 6. The bound condition $\gamma\|\boldsymbol{s}\| - \|h(t, \boldsymbol{s})\| \geq 0$ in (27).

zones are shown in Figs. 5(a) and 5(b). The proposed SAP controller (25) ensures the safety of the sensitive equipment. Meanwhile, according to Fig. 5(c), the collision threat between the spacecraft and the obstacles is avoided. According to Fig. 5, the initial pose configuration and desired pose configuration of the spacecraft satisfy the required Assumptions 2–4. As seen from Fig. 6, the key condition (27) for vanishing disturbances is satisfied, which is an improvement compared with Huang, Yan, and Zhou (2017, Theorem 2, Eq. (59)), Huang, Yan, Zhou, and Yang (2017, Theorem 1, Eq. (69)), and Zhang, Ye, et al. (2019, Theorem 2, Eq. (39)).

7. Conclusions

In this paper, based on the uniformly asymptotically stable theory of nonlinear vanishing perturbation systems, a saturated adaptive pose controller is proposed for the spacecraft on SE(3) to realize the desired pose configuration tracking with the attitude constraints and obstacle-avoidance constraints, input saturation, and disturbances. Based on the dead-zone saturation operation, the relative kinematics and dynamics on SE(3) are constructed. Cancellable potential functions are designed by introducing the warning range for the pose constraints. Then, the SAP pose controller leveraging the cancellable potential functions is proposed to achieve the desired pose configuration tracking under pose constraints. Finally, simulation results demonstrate the efficiency of the proposed integrated pose controller. In future works, the acquisition of attitude information of space obstacles, the pointing deviation of spaceborn equipment, and the underactuated coupling control near Small Bodies will be explored.

References

Brás, Sérgio, Izadi, Maziar, Silvestre, Carlos, Sanyal, Amit, & Oliveira, Paulo (2016). Nonlinear observer for 3D rigid body motion estimation using Doppler measurements. *IEEE Transactions on Automatic Control*, *61*(11), 3580–3585.

Chen, Ti, & Shan, Jinjun (2021). Distributed spacecraft attitude tracking and synchronization under directed graphs. *Aerospace Science and Technology*, *109*, Article 106432.

Dhullipalla, Mani H., Hamrah, Reza, Warier, Rakesh R., & Sanyal, Amit K. (2019). Trajectory generation on SE(3) for an underactuated vehicle with pointing direction constraints. In *2019 American control conference* (pp. 1930–1935). IEEE.

Gui, Haichao, & Vukovich, George (2016). Finite-time output-feedback position and attitude tracking of a rigid body. *Automatica*, *74*, 270–278.

Guo, Yong, Song, Shen-Min, & Li, Xue-Hui (2016). Finite-time output feedback attitude coordination control for formation flying spacecraft without unwinding. *Acta Astronautica*, *122*, 159–174.

Hamrah, Reza, & Sanyal, Amit K. (2022). Finite-time stable tracking control for an underactuated system in SE(3) in discrete time. *International Journal of Control*, *95*(4), 1106–1121.

Henry, David, Zenteno-Torres, Jazmin, Cieslak, Jérôme, Ferreira De Loza, Alejandra, & Dávila, Jorge (2021). A 6-DOF sliding mode fault tolerant control solution for in-orbit autonomous rendezvous. *Aerospace Science and Technology*, *118*, Article 107050.

Horn, Roger A. (1990). The hadamard product. In *Proceedings of symposia in applied mathematics, vol. 40* (p. 88).

Hu, Qinglei, Dong, Hongyang, Zhang, Youmin, & Ma, Guangfu (2015). Tracking control of spacecraft formation flying with collision avoidance. *Aerospace Science and Technology*, *42*, 353–364.

Huang, Xu, Yan, Ye, & Zhou, Yang (2017). Underactuated spacecraft formation reconfiguration with collision avoidance. *Acta Astronautica*, *131*, 166–181.

Huang, Xu, Yan, Ye, Zhou, Yang, & Yang, Yueneng (2017). Dual-quaternion based distributed coordination control of six-DOF spacecraft formation with collision avoidance. *Aerospace Science and Technology*, *67*, 443–455.

Kang, Zeyu, Shen, Qiang, & Wu, Shufan (2020). Constrained attitude control of over-actuated spacecraft subject to instrument pointing direction deviation. *IEEE Control Systems Letters*, *5*(6), 1958–1963.

Kang, Zeyu, Shen, Qiang, Wu, Shufan, & Damaren, Christopher J. (2023). Saturated attitude control of multi-spacecraft systems on SO(3) subject to mixed attitude constraints with arbitrary initial attitude. *IEEE Transactions on Aerospace and Electronic Systems*.

Kang, Zeyu, Wu, Shufan, Huang, Yixin, Zhang, Yi, Shen, Qiang, & Wang, Xiaoliang (2022). Collision avoidance and tracking control of multi-spacecraft under input saturation. In *International conference on guidance, navigation and control* (pp. 3149–3158). Springer.

Khalil, Hassan K. (2002). *Nonlinear systems* (3rd ed.). (pp. 340–346). Upper Saddle River, NJ, USA: Patience Hall.

Kristiansen, Raymond, Nicklasson, Per Johan, & Gravdahl, Jan Tommy (2008). Spacecraft coordination control in 6DOF: Integrator backstepping vs passivity-based control. *Automatica*, *44*(11), 2896–2901.

Kulumani, Shankar, & Lee, Taeyoung (2017). Constrained geometric attitude control on SO(3). *International Journal of Control, Automation and Systems*, *15*(6), 2796–2809.

Lee, Daero, Sanyal, Amit K., & Butcher, Eric A. (2015). Asymptotic tracking control for spacecraft formation flying with decentralized collision avoidance. *Journal of Guidance, Control, and Dynamics*, *38*(4), 587–600.

Lee, Daero, Viswanathan, Sasi Prabhakaran, Holguin, Lee, Sanyal, Amit K., & Butcher, Eric A. (2013). Decentralized guidance and control for spacecraft formation flying using virtual leader configuration. In *2013 American control conference* (pp. 4826–4831). IEEE.
Lee, Daero, & Vukovich, George (2016). Robust adaptive terminal sliding mode control on SE(3) for autonomous spacecraft rendezvous and docking. *Nonlinear Dynamics*, *83*(4), 2263–2279.
Li, Bin, Wang, Yang, Zhang, Kai, & Duan, Guang-Ren (2021). Constrained feedback control for spacecraft reorientation with an optimal gain. *IEEE Transactions on Aerospace and Electronic Systems*, *57*(6), 3916–3926.
Mei, Yafei, Liao, Ying, Gong, Kejie, & Luo, Da (2022). Fuzzy adaptive sliding mode fault estimation and fixed-time fault-tolerant control for coupled spacecraft based on SE(3). *Aerospace Science and Technology*, Article 107673.
Mousavi, Seyyed Hossein, & Khayatian, Alireza (2011). Dead-zone model based adaptive backstepping control for a class of uncertain saturated systems. *IFAC Proceedings Volumes*, *44*(1), 14489–14494.
Shen, Qiang, Yue, Chengfei, Goh, Cher Hiang, Wu, Baolin, & Wang, Danwei (2018). Rigid-body attitude stabilization with attitude and angular rate constraints. *Automatica*, *90*, 157–163.
Sun, Liang, & Huo, Wei (2015). Robust adaptive relative position tracking and attitude synchronization for spacecraft rendezvous. *Aerospace Science and Technology*, *41*, 28–35.
Sun, Liang, Sun, Guang, & Jiang, Jingjing (2022). Disturbance observer-based saturated fixed-time pose tracking for feature points of two rigid bodies. *Automatica*, *144*, Article 110475.
Thakur, Divya, Srikant, Sukumar, & Akella, Maruthi R. (2015). Adaptive attitude-tracking control of spacecraft with uncertain time-varying inertia parameters. *Journal of Guidance, Control, and Dynamics*, *38*(1), 41–52.
Yue, Chengfei, Huo, Tao, Lu, Ming, Shen, Qiang, Li, Chaoyong, Chen, Xueqin, et al. (2023). A systematic method for constrained attitude control under input saturation. *IEEE Transactions on Aerospace and Electronic Systems*.
Zappulla, Richard, Park, Hyeongjun, Virgili-Llop, Josep, & Romano, Marcello (2019). Real-time autonomous spacecraft proximity maneuvers and docking using an adaptive artificial potential field approach. *IEEE Transactions on Control Systems Technology*, *27*(6), 2598–2605.
Zhang, Jianqiao, Biggs, James Douglas, Ye, Dong, & Sun, Zhaowei (2019). Extended-state-observer-based event-triggered orbit-attitude tracking for low-thrust spacecraft. *IEEE Transactions on Aerospace and Electronic Systems*, *56*(4), 2872–2883.
Zhang, Jianqiao, Ye, Dong, Biggs, James D., & Sun, Zhaowei (2019). Finite-time relative orbit-attitude tracking control for multi-spacecraft with collision avoidance and changing network topologies. *Advances in Space Research*, *63*(3), 1161–1175.
Zhang, Hongzhu, Ye, Dong, Xiao, Yan, & Sun, Zhaowei (2022). Adaptive control on SE(3) for spacecraft pose tracking with harmonic disturbance and input saturation. *IEEE Transactions on Aerospace and Electronic Systems*, *58*(5), 4578–4594.

Zeyu Kang was born in Shaanxi, China, in 1994. He received the B.E. and M.E. degrees in control science and engineering from Northwestern Polytechnical University, Xi'an, China, in 2016, and 2019, respectively.

He is currently working toward a Ph.D. degree from the school of Aeronautics and Astronautics, Shanghai Jiao Tong University, Shanghai, China. His research interests include spacecraft control under multiple constraints.

Qiang Shen received his B.E. degree in automation from the Northwestern Polytechnical University, Xi'an, China, in 2010, and the Ph.D. degree in control and instrumentation from Nanyang Technological University, Singapore, in 2016.

From 2015 to 2017, he held a Research Scientist position at Temasek Laboratories, National University of Singapore, Singapore. From 2017 to 2019, he was a Postdoctoral Research Associate with the Mechanical and Aerospace engineering, Arizona State University, Tempe, AZ, USA. Currently, he is an Associate Professor in the School of Aeronautics and Astronautics, Shanghai Jiao Tong University, China. His research interests include spacecraft dynamics and control, fault diagnosis and tolerant control, active model discrimination, and control allocation.

Shufan Wu was born in China, in 1964. He received the B.E. degree in automatic control, the M.E., and Ph.D. degrees in Guidance, Navigation and Control from Nanjing University of Aeronautics and Astronautics (NUAA), Nanjing, China, in 1984, 1987, and 1990, respectively.

He worked as assistant/associate/full professor at NUAA from 1990 till 1998, as a research fellow with TU Braunschweig in Germany (1995–1996), with TU Delft in Netherlands (1999), and with Surrey Space Centre at Surrey University in UK (2000–2002). He served as a Senior/Fellow Engineer with European Space Technology and Research Center (ESTEC) of ESA from 2002 to 2013. He was CTO of the Shanghai Engineering Center for Microsatellites in China from 2013 to 2017. Since 2017, he has been with the School of Aeronautics and Astronautics, Shanghai Jiao Tong University (SAA SJTU), as a Chair Professor. His current research interests include guidance, navigation and control, intelligent microsatellite technology and application, and space science exploration.

Prof. Wu is a Academician of the International Academy of Astronautics (IAA) and an Associate Fellow of the American Institute of Aeronautics and Astronautics (AIAA).

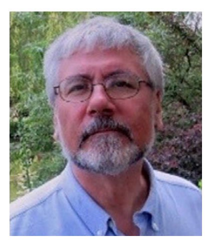

Christopher J. Damaren was born in Toronto, ON, Canada, in 1962. He received the B.A.Sc. degree in engineering science from the University of Toronto, Toronto, in 1985, and the M.A.Sc. and Ph.D. degrees in aerospace engineering from the University of Toronto Institute for Aerospace Studies (UTIAS), North York, ON, Canada, in 1987 and 1990, respectively.

He was an Assistant Professor with the Department of Engineering, Royal Roads Military College, Victoria, BC, Canada, from 1990 to 1995. From 1995 to 1999, he was a Senior Lecturer with the Department of Mechanical Engineering, University of Canterbury, Christchurch, New Zealand. Since 1999, he has been with UTIAS, and is currently a Director and Professor of UTIAS. His current research interests include dynamics and control of space systems.

Prof. Damaren is a Fellow of the Canadian Aeronautics and Space Institute (CASI) and an Associate Fellow of the American Institute of Aeronautics and Astronautics (AIAA).